9. National Conference on Computational Mechanics
MekIT'17
B. Skallerud and H I Andersson (Eds)

A COMPARATIVE STUDY OF BEAM ELEMENT FORMULATIONS FOR NONLINEAR ANALYSIS: COROTATIONAL VS GEOMETRICALLY EXACT FORMULATIONS

KJELL M. MATHISEN[1], YURI BAZILEVS[2], BJØRN HAUGEN[3], TORE A. HELGEDAGSRUD[1], TROND KVAMSDAL[4,5], KNUT M. OKSTAD[5] AND SIV B. RAKNES[1]

[1]Department of Structural Engineering
Norwegian University of Science and Technology (NTNU), Trondheim, Norway
e-mail: Kjell.Mathisen@ntnu.no

[2]Department of Structural Engineering, University of California, San Diego, USA

[3]Department of Mechanical and Industrial Engineering, NTNU, Trondheim, Norway

[4]Department of Mathematical Sciences, NTNU, Trondheim, Norway

[5]Department of Mathematics and Cybernetics, SINTEF Digital, Trondheim, Norway

Key words: Nonlinear finite element analysis, Beam structures, Euler-Bernoulli beams, Timoshenko beams, Geometrically exact beam theory, Corotational elements

Abstract. In this work the geometrically exact three-dimensional beam theory has been used as basis for development of a family of isoparametric higher order large deformation curved beam elements. Geometrically exact three-dimensional beam theory has no restrictions with respect to the magnitude of displacements, rotations and deformations. While reduced integration may be used to alleviate transverse shear and membrane locking in linear and quadratic C^0-continuous Lagrange elements, this does not automatically extend to higher order elements. In this study we demonstrate that uniform reduced numerical quadrature rules may be used to obtain locking-free isoparametric large deformation geometrically exact curved beam elements of arbitrary order. A set of carefully selected numerical examples serves to illustrate and assess the performance of the various geometrically exact elements and compare them with one of the most popular finite element formulations for solving nonlinear beam problems based on the corotational formulation.

1 INTRODUCTION

The finite element (FE) method has been widely used in nonlinear analysis of three-dimensional (3D) curved beam-like structural systems subjected to large displacements and large strains for several decades. Numerous approaches have been proposed, but the vast majority of them have been limited to considering the beam element reference geometry being a straight line. In this work we aim to extend the *geometrically exact* (GE) beam model (see Simo [27] and Simo and Vu-Quoc [28, 29]) based on Reissner's 3D beam theory [24], to model arbitrary shaped curved beam geometry. Several authors, e.g., Stolarski and Belytschko [30] and Ibrahimbegović [16], have observed that increasing the accuracy of the approximated curved beam geometry entails a significant increase in accuracy. The curved 3D GE beam formulation presented herein is able to accommodate large displacements, finite rotations and finite strains. In contrast to the corotational (CR)-type of beam elements (see, e.g., Battini and Pacoste [3, 4], Crisfield [9], Felippa and Haugen [11], and Mathisen and Bergan [20]), it can be easily extended to higher-order beam elements. Saje [26] extended the GE beam model to higher-order two-dimensional (2D) curved beams and Ibrahimbegović [16] to 3D curved beams. However, the latter work was restricted to quadratic hierarchical displacement interpolation. To our knowledge the current work represent the first attempt to extend the GE beam model to an arbitrary order of interpolation. Also our extension of the linearly interpolated straight beam formulation proposed by Simo and Vu-Quoc [28] follows more closely the CR approach since we derive the energy-conjugate strains from a polar decomposition of the deformation tensor rather than defining stress resultants and couples *a priori* and achieving energy-conjugate strain measures through the variational formulation which was employed in the original work.

In this context, our aim is to develop a family of GE 3D beam elements free of locking for the analysis of geometrically nonlinear finite deformation curved beam-like structural systems. In order to do that, we propose an extension of the GE beam model presented in [27, 28, 29], to higher-order Lagrangian-based discretization of both the geometry, displacement, and the rotational fields. To alleviate locking, we have proposed and validated quadrature rules based on uniform reduced integration of the translational and rotational part of the beam model for arbitrary order of interpolation.

This paper is outlined as follows. In Section 2, the GE beam model due to Simo [27] and Simo and Vu-Quoc [28, 29] is presented. Section 3 highlights locking effects in beams together with a presentation of the various enhancements used to alleviate locking. In Section 4, the various proposed GE elements are tested and compared with several 2-noded beam elements based on the CR formulation proposed by Battini and Pacoste [3, 4] on a selection of beam problems. Finally, in Section 5 we summarize and draw conclusions.

2 A GEOMETRICALLY EXACT BEAM MODEL

In this section we consider the continuum basis for a GE beam theory that is optimally suited for computational solution by the FE method. GE beam theory is sometimes referred to as the Reissner's beam theory [24], but strictly speaking, the latter is only exact for a planar beam [23]. The theory presented herein is based on the pioneering work of Simo [27] and Simo and Vu-Quoc [28, 29], that in [29] introduced the still-used terminology GE beam model to indicate that Reissner's theory was recast in a form which is valid for finite rotations. The GE beam model has later been revisited and further developed by numerous authors over more than two decades, e.g., Cardona and Géradin [7] and Ibrahimbegović [16], in which the latter extended the theory to handle curved reference geometry. Beam models of this type have been coined *geometrically exact* because they account, without approximation, for the total deformation and strains.

2.1 Beam geometry in 3D space

The beam is viewed as a 3D body, whose material placement can be described by the line of centroids $\mathcal{B}_0 \subset \mathbb{R}^3$, that has attached at each point a planar non-deformable cross section A_0 in the reference configuration. A local curvilinear coordinate system is chosen to parameterize this line through an arc-length coordinate S along $\mathcal{B}_0$ in the reference configuration. Let $\{\boldsymbol{i}_i(S,t)\}_{i=1,2,3}$ represent a local Cartesian moving frame whose origin is fixed at the centroid at all times, $\boldsymbol{i}_1(S,t)$ remains perpendicular to A and $\{\boldsymbol{i}_\alpha(S,t)\}_{\alpha=2,3}$ span the cross section of the beam in the current configuration. Henceforth, we use the summation convention with Latin indices ranging from 1 to 3 and with Greek indices ranging from 2 to 3. In the reference configuration the orthonormal basis vectors are denoted $\boldsymbol{i}_i^0(S) = \boldsymbol{i}_i(S,0)$ and the associated set of cross section coordinates x_α^0 (see Fig. 1). Let $\boldsymbol{X}(S)$ and $\boldsymbol{x}(S,t)$ define the position of $\mathcal{B}_0$ and $\mathcal{B}$ in the 3D space in the reference and current configuration, respectively:

$$\boldsymbol{x}(S,t) = \boldsymbol{X}(S) + \boldsymbol{u}(S,t), \tag{1}$$

where $\boldsymbol{u}(S,t)$ denote the displacement of $\mathcal{B}_0$ at any time t. We assume that the length of the line of centroids $\mathcal{B}_0$ and $\mathcal{B}$ is L_0 and L, respectively.

Without loss of generality, we assume that; (1) the beam has uniform cross sections, i.e., cross-sectional properties remain constant along the entire length of the beam, (2) the beam reference configuration is stress- and strain-free, and (3) the cross sections are initially normal to $\mathcal{B}_0$, hence:

$$\boldsymbol{i}_1^0(S) = \frac{d\boldsymbol{X}(S)}{dS} = \boldsymbol{X}'(S), \tag{2}$$

where prime denotes the derivative with respect to the arc-length coordinate S.

In accordance with standard hypothesis for beams, we further assume that:

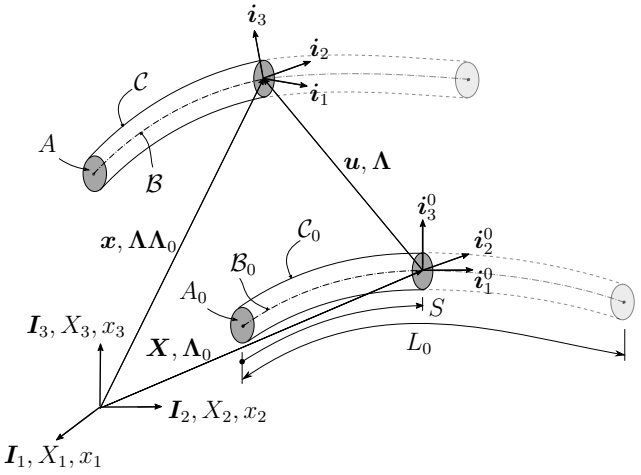

Figure 1: Definition of the various frames and configurations for the GE beam model.

(i) The cross sections remain plane and undeformed in the current configuration, i.e., warping effects are not accounted for.

(ii) The cross sections that initially are normal to $\mathcal{B}_0$ do not necessarily remain normal to the deformed line of centroids $\mathcal{B}$ in the current configuration, i.e., transverse shear deformations are accounted for; hence $\boldsymbol{i}_1(S,t)$ remain normal to A but not necessarily tangent to $\mathcal{B}$.

The orientation of the moving local Cartesian frame $\boldsymbol{i}_i(S,t)$ along $S \in [0,L]$, and through time $t \in [0,T]$ is governed by the orthogonal two-point tensor $\boldsymbol{\Lambda}(S,t)$ such that

$$\boldsymbol{i}_i(S,t) = \boldsymbol{\Lambda}(S,t)\boldsymbol{i}_i^0(S) \Rightarrow \boldsymbol{\Lambda}(S,t) = \boldsymbol{i}_i \otimes \boldsymbol{i}_i^0; \| \boldsymbol{i}_i \| = \| \boldsymbol{i}_i^0 \| = 1 \Rightarrow \boldsymbol{\Lambda}^T\boldsymbol{\Lambda} = \boldsymbol{\Lambda}\boldsymbol{\Lambda}^T = \boldsymbol{I}, \quad (3)$$

where $\boldsymbol{I}$ denote the identity tensor. Defining the reference and current configurations with respect to a global Cartesian frame $\boldsymbol{I}_i$, the above transformation reads:

$$\boldsymbol{i}_i(S,t) = \boldsymbol{\Lambda}(S,t)\boldsymbol{\Lambda}_0(S)\boldsymbol{I}_i \Rightarrow \boldsymbol{\Lambda}_0(S) = \boldsymbol{i}_i^0 \otimes \boldsymbol{I}_i, \quad (4)$$

where $\boldsymbol{\Lambda}_0(S)$ defines the orientation of the local Cartesian frame $\boldsymbol{i}_i^0(S)$ in the reference configuration. The current configuration $\mathcal{C}$ of the 3D beam at any time t will then be uniquely determined by the current position and the rotation of the centroid of the cross section, i.e., the origin of the moving frame:

$$\mathcal{C} = \{\boldsymbol{\varphi} = (\boldsymbol{x}, \boldsymbol{\Lambda}) : [0,L] \times [0,T] \longrightarrow \mathbb{R}^3 \times SO(3)\}, \quad (5)$$

where $SO(3)$ represents the special orthogonal (Lie) group, i.e., the group of all rotations about the origin of $\mathbb{R}^3$ under the operation of composition. As a consequence, the 3D kinematic description of the beam is reduced to a 1D kinematic description with the arc-length coordinate S as the only parameter. With these definitions, the 3D beam geometry in the current configuration may be defined as

$$\boldsymbol{x}^{3\mathrm{D}}(S, x_\alpha^0, t) = \boldsymbol{x}(S,t) + \boldsymbol{p}(S, x_\alpha^0, t), \tag{6}$$

where

$$\boldsymbol{p}(S, x_\alpha^0, t) = \boldsymbol{\Lambda}(S,t)\boldsymbol{p}_0(S, x_\alpha^0) = \boldsymbol{\Lambda}(S,t) x_\alpha^0 \boldsymbol{i}_\alpha^0(S). \tag{7}$$

$\boldsymbol{p}$ and $\boldsymbol{p}_0$ denote the cross section position vector along $\mathcal{B}$, i.e., the position of a point P relative to the centroid within a cross section, in the current and reference configuration, respectively. Herein, we only consider quasi-static analysis of beam problems. However, the kinematic description presented in this section is identical for static and dynamic problems. For that reason, "time" and "pseudo-time" as well as "time step", "incremental step" and "load step" are used as equivalents throughout this work.

2.2 Parameterization of finite 3D rotations

The principal difficulty by representing 3D finite rotations by an orthogonal tensor $\boldsymbol{\Lambda}$ is due to the fact that $SO(3)$ is not a linear (vector) space, but rather a manifold, hence consistent linearization and update procedures are no longer straightforward. In the context of time-independent (static) analysis, Ibrahimbegović [17] overcame this problem by reparameterizing the configuration space of the beam by making use of the so-called rotation vector $\boldsymbol{\theta}$, defined by

$$\boldsymbol{\theta} = \theta \boldsymbol{e}, \tag{8}$$

where $\boldsymbol{e}$ is a unit vector defining the axis of rotation and $\theta = \sqrt{\theta_1^2 + \theta_2^2 + \theta_3^2}$ is the magnitude of the rotation vector. The relation between $\boldsymbol{\Lambda}$ and $\boldsymbol{\theta}$ is governed by the Rodriguez formula which represents a closed form solution of the exponential mapping

$$\boldsymbol{\Lambda} = \exp[\widetilde{\boldsymbol{\theta}}] = \boldsymbol{I} + \frac{\sin\theta}{\theta}\widetilde{\boldsymbol{\theta}} + \frac{1-\cos\theta}{\theta^2}\widetilde{\boldsymbol{\theta}}\widetilde{\boldsymbol{\theta}}, \tag{9}$$

where $\widetilde{\boldsymbol{\theta}}$ denote the skew-symmetric tensor for which $\boldsymbol{\theta}$ is the axial vector, i.e.:

$$\boldsymbol{\theta} = [\theta_1, \theta_2, \theta_3] \Rightarrow \widetilde{\boldsymbol{\theta}} = \mathrm{skew}[\boldsymbol{\theta}] = \begin{bmatrix} 0 & -\theta_3 & \theta_2 \\ \theta_3 & 0 & -\theta_1 \\ -\theta_2 & \theta_1 & 0 \end{bmatrix}. \tag{10}$$

With such a parameterization, the configuration space $\mathcal{C}$ becomes a linear space:

$$\mathcal{C} = \{\boldsymbol{\varphi} = (\boldsymbol{x}, \boldsymbol{\Lambda}) : [0, L] \times [0, T] \longrightarrow \mathbb{R}^3 \times \mathbb{R}^3\}. \tag{11}$$

The admissible variation $\delta\boldsymbol{\Lambda}$ of the orthogonal tensor of finite rotations can be constructed by making use of the exponential mapping

$$\delta\boldsymbol{\Lambda} = \widetilde{\delta\boldsymbol{w}}\boldsymbol{\Lambda} = \boldsymbol{\Lambda}\widetilde{\delta\boldsymbol{\psi}}. \tag{12}$$

Physically, $\widetilde{\delta\boldsymbol{w}}$ and $\widetilde{\delta\boldsymbol{\psi}}$ represent infinitesimal spatial and material rotations superposed onto the existing rotation $\boldsymbol{\Lambda}$. The spatial spin variables, $\delta\boldsymbol{w}$, are also related to the variation of the rotational vector through (see [17])

$$\delta\boldsymbol{w} = \boldsymbol{T}_s(\boldsymbol{\theta})\,\delta\boldsymbol{\theta}, \tag{13}$$

where

$$\boldsymbol{T}_s(\boldsymbol{\theta}) = \boldsymbol{I} + \frac{1-\cos\theta}{\theta^2}\widetilde{\boldsymbol{\theta}} + \frac{\theta-\sin\theta}{\theta^3}\widetilde{\boldsymbol{\theta}}\widetilde{\boldsymbol{\theta}}. \tag{14}$$

If the rotational vector is used as parameterization, the rotations become additive and are updated at each iteration. However, the relation in Eq. (13) cease to be bijection for $\theta = 2n\pi$. Consequently, with the parameterization using the rotational vector, the angle of rotation is limited to 2π. In large deformation analysis, and especially in dynamic large deformation analysis, angles of rotation can become much larger than 2π. In order to overcome this limitation, Cardona and Géradin [7] and Ibrahimbegović *et al.* [17] proposed to apply Eq. (13) only within an increment and introduced the concept of incremental rotation vector, based on the following update procedure:

(i) At the beginning at the time step $(n+1)$, i.e., for iteration $i = 0$, the incremental rotation vector is set to zero:

$$\boldsymbol{\theta}^0_{n+1} = \boldsymbol{0}. \tag{15}$$

(ii) At the i^{th} iteration the incremental rotation vector is updated additively

$$\boldsymbol{\theta}^i_{n+1} = \boldsymbol{\theta}^{i-1}_{n+1} + \Delta\boldsymbol{\theta}, \tag{16}$$

where $\Delta\boldsymbol{\theta}$ represents the iterative change of the incremental rotation vector.

(iii) The corresponding orthogonal tensor $\boldsymbol{\Lambda}$ is updated using exponential mapping

$$\boldsymbol{\Lambda}^i_{n+1} = \exp[\widetilde{\boldsymbol{\theta}^i_{n+1}}]\boldsymbol{\Lambda}_n. \tag{17}$$

Hence, additive updates still apply within each time step and the amplitude of the rotations are thus just limited within each time step. Alternatively, if the spatial spin variables are used to parameterize the finite rotations, the update is performed according to

$$\boldsymbol{\Lambda}^i_{n+1} = \exp[\widetilde{\Delta\boldsymbol{w}}]\boldsymbol{\Lambda}^{i-1}_{n+1}, \tag{18}$$

where $\Delta\boldsymbol{w}$ denote the corresponding iterative change of the spatial spin variables.

2.3 Strain measures

In contrast to previous works [7, 16, 17, 23, 24, 27, 28, 29], where energy-conjugate strain measures were based on stress resultants defined *a priori*, Auricchio *et al.* [1] derived a GE beam model in which proper strain measures at any point of the beam in $\mathcal{C}$ were obtained by a polar decomposition of the deformation gradient $\boldsymbol{F}$. With the definition of the 3D geometry in $\mathcal{C}$, see Eq. (6), the deformation gradient may be expressed as

$$\boldsymbol{F} = \frac{\partial \boldsymbol{x}^{3\mathrm{D}}}{\partial x_i^0} \otimes \boldsymbol{i}_i^0 = \left(\boldsymbol{x}' + \boldsymbol{\Lambda}' x_\alpha^0 \boldsymbol{i}_\alpha^0\right) \otimes \boldsymbol{i}_1^0 + \boldsymbol{i}_\alpha \otimes \boldsymbol{i}_\alpha^0. \tag{19}$$

Utilizing Eq. (12), the derivative of the rotation tensor $\boldsymbol{\Lambda}$ with respect to S may be expressed as

$$\boldsymbol{\Lambda}' = \widetilde{\boldsymbol{\kappa}}\boldsymbol{\Lambda} \Leftrightarrow \widetilde{\boldsymbol{\kappa}} = \boldsymbol{\Lambda}'\boldsymbol{\Lambda}^T, \tag{20}$$

where $\widetilde{\boldsymbol{\kappa}} = \widetilde{\boldsymbol{\kappa}}(S)$ is a skew-symmetric tensor represented by the axial vector $\boldsymbol{\kappa}$ denoting the spatial rotational (torsional and bending) strains, i.e., the spatial curvature. Furthermore, adding and subtracting the tensor $\boldsymbol{i}_1 \otimes \boldsymbol{i}_1^0$ to the right-hand-side and recognizing that $\boldsymbol{i}_i \otimes \boldsymbol{i}_i^0 = \boldsymbol{\Lambda}$, we may rewrite Eq. (19) and make a material polar decomposition of $\boldsymbol{F}$

$$\boldsymbol{F} = \boldsymbol{\Lambda}\left\{\boldsymbol{I} + \left[\boldsymbol{\Lambda}^T\left(\boldsymbol{x}' - \boldsymbol{i}_1\right) + \boldsymbol{\Lambda}^T\widetilde{\boldsymbol{\kappa}} x_\alpha^0 \boldsymbol{i}_\alpha^0\right] \otimes \boldsymbol{i}_1^0\right\} = \boldsymbol{\Lambda}\boldsymbol{U}. \tag{21}$$

In Eq. (21), $\boldsymbol{U}$ defines the right (current local) stretch tensor from which we may derive the Biot strain measure $\boldsymbol{B}$ (often referred to as the Jaumann strains), that are objective corotated engineering strains independent of rigid body displacements

$$\boldsymbol{B} = \boldsymbol{\Lambda}^T\boldsymbol{F} - \boldsymbol{I} = \boldsymbol{U} - \boldsymbol{I} = \boldsymbol{\varepsilon} \otimes \boldsymbol{i}_1 \quad \text{with} \quad \boldsymbol{\varepsilon} = \boldsymbol{\Lambda}^T\left(\boldsymbol{\gamma} + \widetilde{\boldsymbol{\kappa}}\boldsymbol{p}\right) = \boldsymbol{\Gamma} + \widetilde{\boldsymbol{K}}\boldsymbol{p}_0, \tag{22}$$

where $\boldsymbol{\varepsilon}$ represents a generalized convected strain measure, $\boldsymbol{\gamma}$ the translational (axial and transverse shear) spatial strains and $\boldsymbol{\kappa}$ the rotational (torsional and bending) spatial curvature strain vector. The corresponding convected material strains are represented by upper case letters $\boldsymbol{\Gamma}$ and $\boldsymbol{K}$. The relationship between the material and spatial forms may then be expressed as

$$\begin{aligned} \boldsymbol{\Gamma} &= \boldsymbol{\Lambda}^T\boldsymbol{\gamma} \quad \text{with} \quad \boldsymbol{\gamma} = \boldsymbol{x}' - \boldsymbol{i}_1, \\ \boldsymbol{K} &= \boldsymbol{\Lambda}^T\boldsymbol{\kappa} \quad \text{with} \quad \boldsymbol{\kappa} = \boldsymbol{T}_s(\boldsymbol{\theta})\boldsymbol{\theta}'. \end{aligned} \tag{23}$$

A physical interpretation of the spatial strain measures is that the components of $\boldsymbol{\gamma}$ represent the true axial and transverse shear strain measures with respect to the current moving frame $\boldsymbol{i}_i(S,t)$, e.g., γ_1 represents the elongation of an infinitesimal fiber in the direction normal to the cross section while γ_2 and γ_3 are the corresponding transverse shear strains. Similarly, the three components of $\boldsymbol{\kappa}$, represents the true torsional (κ_1) and bending strain measures (κ_2 and κ_3) with respect to the moving frame.

2.4 Stress resultants, constitutive equations and balance laws

Work conjugate with the strain measures in Eq. (23), we define material and spatial stress resultants and couples, $\boldsymbol{N}, \boldsymbol{M}$ and $\boldsymbol{n}, \boldsymbol{m}$, where the latter are obtained by a push-forward of the convected resultants and couples:

$$\boldsymbol{n} = \boldsymbol{\Lambda N} \quad \text{and} \quad \boldsymbol{m} = \boldsymbol{\Lambda M}. \tag{24}$$

The first component of the force resultants $\boldsymbol{n}, \boldsymbol{N}$ denotes the axial force in the direction of $\boldsymbol{i}_1, \boldsymbol{i}_1^0$, while component 2 and 3 denote the transverse shear forces in the directions of $\boldsymbol{i}_\alpha, \boldsymbol{i}_\alpha^0$, respectively. Similarly, the first component of the stress couples $\boldsymbol{m}, \boldsymbol{M}$ denotes the torsional moment about the axis of $\boldsymbol{i}_1, \boldsymbol{i}_1^0$, while component 2 and 3 denote the bending moments about the axes of $\boldsymbol{i}_\alpha, \boldsymbol{i}_\alpha^0$, respectively. For a hyperelastic material the convected resultants may be obtained from a strain energy function $\Psi(\boldsymbol{\Gamma}, K)$ through the relations

$$\boldsymbol{N} = \frac{\partial \Psi(\boldsymbol{\Gamma}, K)}{\partial \boldsymbol{\Gamma}} \quad \text{and} \quad \boldsymbol{M} = \frac{\partial \Psi(\boldsymbol{\Gamma}, K)}{\partial \boldsymbol{K}}. \tag{25}$$

In our study we assume that we have a linear isotropic relation between stresses and strains. This results in a St. Venant–Kirchhoff-type constitutive relation that may be expressed in terms of E and G, denoting the Young's and the shear modulus, respectively. The corresponding resultant constitutive laws reads

$$\boldsymbol{N} = \begin{bmatrix} N^1 \\ N^2 \\ N^3 \end{bmatrix} = \begin{bmatrix} EA_0 & 0 & 0 \\ 0 & G\bar{A}_{02} & 0 \\ 0 & 0 & G\bar{A}_{03} \end{bmatrix} \begin{bmatrix} \Gamma_1 \\ \Gamma_2 \\ \Gamma_3 \end{bmatrix} = \boldsymbol{C}_N \boldsymbol{\Gamma} \text{ with } \begin{matrix} N^i = \boldsymbol{N} \cdot \boldsymbol{i}_i^0 \\ \Gamma_i = \boldsymbol{\Gamma} \cdot \boldsymbol{i}_i^0 \end{matrix}, \tag{26}$$

and

$$\boldsymbol{M} = \begin{bmatrix} M^1 \\ M^2 \\ M^3 \end{bmatrix} = \begin{bmatrix} GI_T & 0 & 0 \\ 0 & EI_{33} & -EI_{32} \\ 0 & -EI_{23} & EI_{22} \end{bmatrix} \begin{bmatrix} K_1 \\ K_2 \\ K_3 \end{bmatrix} = \boldsymbol{C}_M \boldsymbol{K} \text{ with } \begin{matrix} M^i = \boldsymbol{M} \cdot \boldsymbol{i}_i^0 \\ K_i = \boldsymbol{K} \cdot \boldsymbol{i}_i^0 \end{matrix}, \tag{27}$$

where $G\bar{A}_{0\alpha}$ denotes the reduced cross section shear area in the direction of $\boldsymbol{i}_\alpha^0$, I_T the torsional stiffness and $I_{\alpha\beta} = \int_{A_0} x_\alpha^0 x_\beta^0 dA$ the cross section second moment of area.

The corresponding relation between the spatial stress resultants and couples and the energy conjugate strains $\boldsymbol{\gamma}$ and $\boldsymbol{\kappa}$, is obtained by combining Eqs. (23), (24), (26) and (27)

$$\boldsymbol{n} = \boldsymbol{\Lambda C}_N \boldsymbol{\Lambda}^T \boldsymbol{\gamma} \quad \text{and} \quad \boldsymbol{m} = \boldsymbol{\Lambda C}_M \boldsymbol{\Lambda}^T \boldsymbol{\kappa}. \tag{28}$$

As shown by Reissner [23, 24], Simo [27] and Simo and Vu-Quoc [28, 29], the beam balance equations can be obtained without any simplifying hypothesis regarding geometry, and size of displacements and rotations, hence, this theory is referred to as GE. If we consider $\bar{\boldsymbol{n}}$ and $\bar{\boldsymbol{m}}$ to be the externally applied force and moment per unit length the

time-independent linear and angular momentum balance (strong form) equations for the GE beam model reads:

$$\boldsymbol{n}' + \bar{\boldsymbol{n}} = \boldsymbol{0} \quad \text{and} \quad \boldsymbol{m}' + \boldsymbol{x}' \times \boldsymbol{n} + \bar{\boldsymbol{m}} = \boldsymbol{0}. \tag{29}$$

A unique strong form solution must satisfy the balance equations stated in Eq. (29) supplemented with the boundary conditions:

$$\begin{aligned} \boldsymbol{x} &= \bar{\boldsymbol{x}} \ \text{ on } \ \mathcal{B}_x^{\varphi} \quad \text{and} \quad \boldsymbol{\Lambda} = \bar{\boldsymbol{\Lambda}} \ \text{ on } \ \mathcal{B}_{\Lambda}^{\varphi}, \\ \boldsymbol{n} &= \bar{\boldsymbol{n}} \ \text{ on } \ \mathcal{B}_n^{\sigma} \quad \text{and} \quad \boldsymbol{m} = \bar{\boldsymbol{m}} \ \text{ on } \ \mathcal{B}_m^{\sigma}, \end{aligned} \tag{30}$$

where $\mathcal{B}_x^{\varphi}$, $\mathcal{B}_{\Lambda}^{\varphi}$, $\mathcal{B}_n^{\sigma}$ and $\mathcal{B}_m^{\sigma}$ denote the part of the beam where displacements, rotations, stress resultants and couples are prescribed, respectively.

2.5 Variational equations

The variational or weak form of the static equilibrium equations states that the solution to the beam problem (29) with the associated boundary conditions (30) is the motion $\boldsymbol{\varphi} = (\boldsymbol{x}, \boldsymbol{\Lambda}) \in \mathcal{S}$ that satisfies the principle of virtual work, which states that

$$\delta W = \delta W^{\text{int}} + \delta W^{\text{ext}}, \tag{31}$$

for all admissible virtual variations $\delta\boldsymbol{\varphi} = (\delta\boldsymbol{x}, \delta\boldsymbol{w})$. The internal virtual work carried out by the spatial stress resultants and couples over the associated admissible variations in the current configuration is given by (for more details see, e.g., Cardona and Géradin [7] or Helgedagsrud *et al.* [12]):

$$\delta W^{\text{int}} = \delta W^{\text{int}}(\boldsymbol{\varphi}, \delta\boldsymbol{\varphi}) = \int_L \{(\delta\boldsymbol{x}' + \boldsymbol{x}' \times \delta\boldsymbol{w}) \cdot \boldsymbol{n} + \delta\boldsymbol{w}' \cdot \boldsymbol{m}\} d\ell. \tag{32}$$

The external virtual work due to the distributed externally applied force and moment per unit length may be expressed as:

$$\delta W^{\text{ext}} = \delta W^{\text{ext}}(\delta\boldsymbol{\varphi}) = -\int_L \{\delta\boldsymbol{x} \cdot \bar{\boldsymbol{n}} + \delta\boldsymbol{w} \cdot \bar{\boldsymbol{m}}\} d\ell. \tag{33}$$

Combining the internal and external virtual work terms, we obtain the following spatial form of the variational formulation of the GE beam model: Find $\boldsymbol{\varphi} = (\boldsymbol{x}, \boldsymbol{\Lambda}) \in \mathcal{S}$, such that $\forall \delta\boldsymbol{\varphi} = (\delta\boldsymbol{x}, \delta\boldsymbol{w}) \in \mathcal{V}$:

$$\int_L \{(\delta\boldsymbol{x}' + \boldsymbol{x}' \times \delta\boldsymbol{w}) \cdot \boldsymbol{n} + \delta\boldsymbol{w}' \cdot \boldsymbol{m}\} d\ell = \int_L \{\delta\boldsymbol{x} \cdot \bar{\boldsymbol{n}} + \delta\boldsymbol{w} \cdot \bar{\boldsymbol{m}}\} d\ell. \tag{34}$$

In the formulation, $\mathcal{S}$ and $\mathcal{V}$ are suitably defined trial and test function spaces for the GE beam problem. Strictly speaking, the space of kinematically admissible variations for

the GE beam model is the tangent space at $\boldsymbol{\varphi}$ to the abstract configuration manifold $\mathcal{C}$, which is denoted $\mathcal{T}_{\varphi}\mathcal{C}$. Hence, in general $\delta\boldsymbol{\varphi}$ must be a member of the tangent space $\mathcal{T}_{\varphi}\mathcal{C}$. However, as pointed out in Section 2.2, when $\delta\boldsymbol{w}$ is an infinitesimal rotation superposed on the finite rotation $\boldsymbol{\Lambda}$ and the update is performed as an exponential map, the space of admissible variations is defined as:

$$\mathcal{V} = \{\delta\boldsymbol{\varphi} = (\delta\boldsymbol{x}, \delta\boldsymbol{w}) : [0,L]\times[0,T] \in \mathbb{R}^3\times\mathbb{R}^3 | \delta\boldsymbol{x} = \boldsymbol{0} \text{ on } \mathcal{B}_x^{\varphi} \text{ and } \delta\boldsymbol{w} = \boldsymbol{0} \text{ on } \mathcal{B}_{\Lambda}^{\varphi}\}. \quad (35)$$

2.6 Linearized variational equations

The virtual work equations for the finite deformation GE beam model are in general highly nonlinear. For this reason the problem is reduced to a set of nonlinear algebraic equations, whose solution is obtained utilizing an incremental-iterative Newton–Raphson approach. In order to obtain the consistent tangent of Newton's method, i.e., the tangent granting quadratic convergence rate, a consistent linearization of the associated variational equations must be performed. The incremental virtual work results in two contributions to the tangent stiffness, the material and geometrical part. With the expressions for the incremental and linearized virtual spatial strain measures at hand the material part is obtained by keeping the geometry constant varying the material resultants

$$\int_L \{(\delta\boldsymbol{x}' + \boldsymbol{x}'\times\delta\boldsymbol{w})\cdot\boldsymbol{\Lambda}\boldsymbol{C}_N\boldsymbol{\Lambda}^T(\Delta\boldsymbol{x}' + \boldsymbol{x}'\times\Delta\boldsymbol{w}) + (\delta\boldsymbol{w}')\cdot\boldsymbol{\Lambda}\boldsymbol{C}_M\boldsymbol{\Lambda}^T\Delta\boldsymbol{w}'\}d\ell, \quad (36)$$

whereas the geometric part is obtained keeping the material properties constant while varying the geometry

$$\int_L \{[(\delta\boldsymbol{x}' + \boldsymbol{x}'\times\delta\boldsymbol{w})\times\Delta\boldsymbol{w} - \delta\boldsymbol{w}\times\Delta\boldsymbol{x}']\cdot\boldsymbol{n} + (\delta\boldsymbol{w}'\times\Delta\boldsymbol{w})\cdot\boldsymbol{m}\}d\ell. \quad (37)$$

2.7 Discrete formulation

In this work we assume that standard Lagrangian basis functions are used to discretize both the geometry in the reference and the current configuration, $\boldsymbol{X}$ and $\boldsymbol{x}$, and the virtual and incremental displacement and rotational fields, $\delta\boldsymbol{\varphi} = (\delta\boldsymbol{x}, \delta\boldsymbol{w})$ and $\Delta\boldsymbol{\varphi} = (\Delta\boldsymbol{x}, \Delta\boldsymbol{w})$, of each individual element of the centroidal line $\mathcal{B}_0$:

$$\begin{aligned} &\boldsymbol{X}^h = \sum_{A=1}^{n_n} R_A\boldsymbol{X}_A, \quad \boldsymbol{x}^h = \sum_{A=1}^{n_n} R_A\boldsymbol{x}_A, \quad \delta\boldsymbol{x}^h = \sum_{A=1}^{n_n} R_A\delta\boldsymbol{x}_A, \\ &\delta\boldsymbol{w}^h = \sum_{A=1}^{n_n} R_A\delta\boldsymbol{w}_A, \quad \Delta\boldsymbol{x}^h = \sum_{A=1}^{n_n} R_A\Delta\boldsymbol{x}_A \text{ and } \Delta\boldsymbol{w}^h = \sum_{A=1}^{n_n} R_A\Delta\boldsymbol{w}_A, \end{aligned} \quad (38)$$

where n_n is the number of nodes associated with the element, R_A is the standard Lagrangian basis function accompanying node A, whereas $\boldsymbol{X}_A$, $\boldsymbol{x}_A$, $\delta\boldsymbol{x}_A$, $\delta\boldsymbol{w}_A$, $\Delta\boldsymbol{x}_A$ and $\Delta\boldsymbol{w}_A$ are the corresponding reference and current coordinate, virtual and incremental displacement and rotation parameter, respectively.

The Galerkin formulation of Eq. (34) is obtained by restricting the trial and test function sets to their finite dimensional counterpart comprised of Lagrange suitable basis functions as: Find $\boldsymbol{\varphi}^h = (\boldsymbol{x}^h, \boldsymbol{\Lambda}^h) \in \mathcal{S}^h$, such that $\forall \delta\boldsymbol{\varphi}^h = (\delta\boldsymbol{x}^h, \delta\boldsymbol{w}^h) \in \mathcal{V}^h$:

$$\int_L \{[\delta(\boldsymbol{x}^h)' + (\boldsymbol{x}^h)' \times \delta\boldsymbol{w}^h] \cdot \boldsymbol{n}^h + \delta(\boldsymbol{w}^h)' \cdot \boldsymbol{m}^h\} d\ell = \int_L \{\delta\boldsymbol{x}^h \cdot \bar{\boldsymbol{n}} + \delta\boldsymbol{w}^h \cdot \bar{\boldsymbol{m}}\} d\ell, \tag{39}$$

where $\boldsymbol{n}^h$ and $\boldsymbol{m}^h$, are the current spatial stress resultants and couples derived from the discretized solution $\boldsymbol{\varphi}^h = (\boldsymbol{x}^h, \boldsymbol{\Lambda}^h)$. The matrix counterpart of the discrete form of the variational equations may be written on compact form as:

$$\sum_{A=1}^{n_n} \delta\mathbf{d}_A (\mathbf{F}_A^{\text{int}} - \mathbf{F}_A^{\text{ext}}) = \mathbf{0}, \tag{40}$$

where $\mathbf{d}_A = [\boldsymbol{x}_A, \boldsymbol{w}_A]^T$ denotes the vectors of nodal displacement and rotation unknowns, and $\mathbf{F}_A^{\text{int}}$ and $\mathbf{F}_A^{\text{ext}}$ the vectors of internal and external nodal forces related to node A, respectively:

$$\mathbf{F}_A^{\text{int}} = \int_L \mathbf{B}_A^T \mathbf{r} d\ell \quad \text{with} \quad \mathbf{B}_A = \begin{bmatrix} R_A' \mathbf{I}_3 & \mathbf{0} \\ R_A \widetilde{\boldsymbol{x}}' & R_A' \mathbf{I}_3 \end{bmatrix} \quad \text{and} \quad \mathbf{r} = \begin{Bmatrix} \boldsymbol{n}^h \\ \boldsymbol{m}^h \end{Bmatrix}, \tag{41}$$

and

$$\mathbf{F}_A^{\text{ext}} = \int_L R_A \mathbf{I}_6 \bar{\mathbf{r}} d\ell \quad \text{with} \quad \bar{\mathbf{r}} = \begin{Bmatrix} \bar{\boldsymbol{n}} \\ \bar{\boldsymbol{m}} \end{Bmatrix}, \tag{42}$$

where $\mathbf{I}_k = \lceil 1, 1, \ldots, 1 \rfloor$ is a diagonal unit matrix of dimension k, and $\widetilde{\boldsymbol{x}}'$ is a skew-symmetric matrix whose axial vector is $\boldsymbol{x}'$.

Similarly, the incremental solution, $\Delta\boldsymbol{\varphi}^h = (\Delta\boldsymbol{x}^h, \Delta\boldsymbol{w}^h) \in \mathcal{V}^h$, of the Galerkin formulation associated with the linearized form of Eqs. (36) and (37) is found from its associated discrete approximation that on matrix form can be written:

$$\sum_{A=1}^{n_n} \sum_{B=1}^{n_n} \delta\mathbf{d}_A \{(\mathbf{F}_A^{\text{int}} - \mathbf{F}_A^{\text{ext}}) + (\mathbf{K}_{AB}^{\text{m}} - \mathbf{K}_{AB}^{\text{g}}) \Delta\mathbf{d}_B\} = \mathbf{0}. \tag{43}$$

The material and geometric stiffness matrices, $\mathbf{K}_{AB}^{\text{m}}$ and $\mathbf{K}_{AB}^{\text{g}}$, are obtained by substituting the discrete approximation counterparts of the virtual and incremental displacements from Eq.(38) into Eqs. (36) and (37):

$$\mathbf{K}_{AB}^{\text{m}} = \int_L \mathbf{B}_A^T \mathbf{C} \mathbf{B}_B d\ell \quad \text{with} \quad \mathbf{C} = \begin{bmatrix} \boldsymbol{C}_N & \mathbf{0} \\ \mathbf{0} & \boldsymbol{C}_M \end{bmatrix}, \tag{44}$$

and with some manipulations (see, e.g., Simo and Vu-Quoc [28, 29])

$$\mathbf{K}^{\mathrm{g}}_{AB} = \int_L \mathbf{G}_A^T \mathbf{H} \mathbf{G}_B d\ell \quad \text{with} \quad \mathbf{G}_A = \begin{bmatrix} R'_A \mathbf{I}_3 & \mathbf{0} \\ \mathbf{0} & R'_A \mathbf{I}_3 \\ \mathbf{0} & R_A \mathbf{I}_3 \end{bmatrix}$$
$$\text{and} \quad \mathbf{H} = \begin{bmatrix} \mathbf{0} & \mathbf{0} & -\widetilde{\boldsymbol{n}}^h \\ \mathbf{0} & \mathbf{0} & -\widetilde{\boldsymbol{m}}^h \\ \widetilde{\boldsymbol{n}}^h & \mathbf{0} & (\boldsymbol{n}^h \otimes \boldsymbol{x}' - \boldsymbol{x}' \boldsymbol{n}^h \mathbf{I}_3) \end{bmatrix}. \tag{45}$$

We recall again that in the expression for $\mathbf{H}$, $\widetilde{\boldsymbol{n}}^h$ and $\widetilde{\boldsymbol{m}}^h$ are the skew-symmetric matrices whose axial vectors are $\boldsymbol{n}^h$ and $\boldsymbol{m}^h$, respectively.

It is noted that the final form of the tangent stiffness $\mathbf{K}^{\mathrm{t}} = \mathbf{K}^{\mathrm{m}} + \mathbf{K}^{\mathrm{g}}$, in general, is nonsymmetric. Since symmetry of the material part follows from the symmetry of the constitutive matrix $\mathbf{C}$, the lack of symmetry stems from the geometric part. As pointed out by Simo and Vu-Quoc [28, 29], for conservative loading at an equilibrium state the tangent stiffness is symmetric. However, in general, at non-equilibrated configurations, the tangent stiffness is nonsymmetric. The reason for that is that the configuration space, $\mathcal{T}_\varphi \mathcal{C}$, is a manifold. Our numerical studies has revealed that replacing the nonsymmetric geometric stiffness by its symmetric counterpart will not jeopardize the quadratic convergence rate expected in the Newton iterations.

Parameterizing the finite rotations with the incremental rotation vector, $\boldsymbol{\theta}$ (see Section 2.2), rather than the spatial spin tensor, $\boldsymbol{w}$, yields similar expressions for the tangent stiffness matrices and the out of balance force vector, and may be found in Ibrahimbegović *et al.* [17].

3 LOCKING EFFECTS IN BEAMS

It is well-known that purely displacement-based isoparametric, especially low-order, elements are often affected by spurious strains and stresses which lead to an overestimation of the stiffness. As a consequence, the primary variables like displacements will be underestimated. In the context of curved beam elements, this implies that both spurious transverse shear and axial (membrane) strains may develop in bending dominated problems, consequently the element will have no ability to capture the state of (transverse) shear-free or inextensional bending. The corresponding locking phenomena denoted transverse shear and membrane locking, in general reduces the accuracy and slows down the convergence as the ratio between thickness to length (for straight members) or thickness to radius of curvature (for curved beams) approaches zero. From the definition of the translational spatial strains (23) for the GE elements we observe that $\boldsymbol{\gamma}^h$ is obtained by subtracting the normal to the cross section $\boldsymbol{i}_1^h$ from the arc-length derivative of the discrete line of centroids $\mathcal{B}^h$ in the current configuration. In the following, we investigate whether $\boldsymbol{\gamma}^h$, i.e., the axial and the transverse shear strains vanish when the element is subjected to a state of pure bending. Without loss of generality we consider an initially

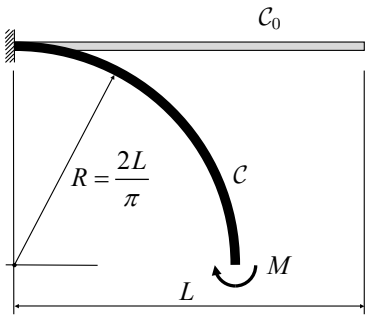

Figure 2: Initial and deformed configuration of a cantilever subjected to a concentrated end moment.

2D straight beam of length L with a rectangular cross section ($A = bh$, with $b = 1$ and $h = 10^{-\rho}$) clamped at one end and subjected to a concentrated moment M at the free end (see Fig. 2). We assume that $L = 1$, $\rho = 3$, $E = 24 \times 10^9$ and $M = \pi EI/2L = \pi$, for which the closed form solution is represented by a quarter of a circle. Fig. 3 shows the resulting distribution of axial and transverse shear strains obtained when the cantilever is discretized with a single GE element of order $p = 1, 2, 3$ and 4, respectively. We observe that all elements sample the exact solution ($\boldsymbol{\gamma} = \mathbf{0}$) at the Gauss points ($n_g = p$) corresponding to uniform reduced integration (URI). We also observe that the amplitudes of the spurious membrane and shear strains reduces dramatically as the order of the interpolant is increased. The ability of the curved Lagrange C^0 isoparametric beam elements to alleviate spurious transverse shear and axial strains with URI was first explored and reported by Stolarski and Belytschko [30] for quadratic and cubic interpolated elements.

In order to evaluate an elements propensity of locking, Hughes [13] introduced an heuristic approach, the so-called *constraint count* method. This method relies on the constraint ratio, r, which is defined as the ratio of the total number of equilibrium equations (n_{eq}) to the total number of constraint equations (n_c):

$$r = \frac{n_{eq}}{n_c}. \tag{46}$$

In order to investigate whether an element is prone to locking, the constraint ratio, r, of the continuous problem is compared with the constraint ratio, r^h, of the discretized problem in the limit of infinite number of elements, $n_e \to \infty$:

$$r^h = \lim_{n_e \to \infty} \frac{n_u^e}{n_c^e}. \tag{47}$$

Here n_u^e denotes the number of unknowns added to the system by adding one more element to a uniform mesh of an infinite number of elements, while n_c^e is the corresponding number of constraints added by this element. Thus, n_c^e is related to the number of quadrature points, n_g, where the constraints are to be evaluated.

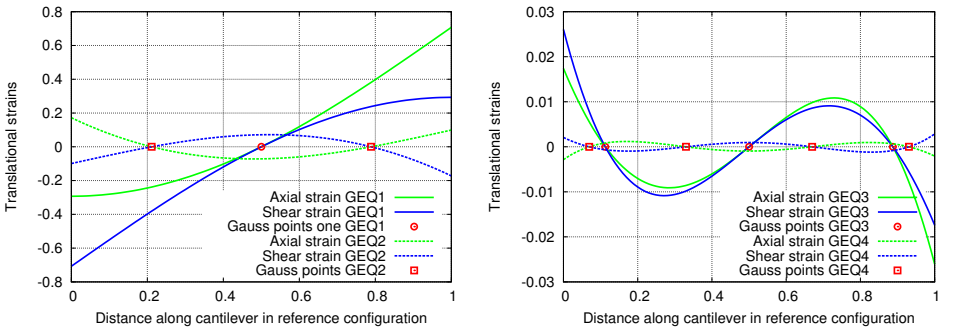

a) b)

Figure 3: Discrete translational strain fields obtained when the cantilever beam subjected to a concentrated end moment is discretized with one single GE element of order $p = 1, 2, 3$ and 4, respectively: a) Solutions for $p = 1$ and 2, denoted GEQ1 and GEQ2, respectively, and b) solutions for $p = 3$ and 4, denoted GEQ3 and GEQ4, respectively.

For an element with $r^h < r$, and especially with $r^h < 1$ (which implies that there are more constraints added than unknowns), the propensity of locking is high. In contrast when $r^h > r$, this indicate that there are too few constraints to approximate the constraint accurately. Consequently, the optimal element satisfy the criterion $r^h = r$.

As pointed out in [30], when investigating the locking behavior of curved C^0 beams for higher-order elements there exists an interrelationship between transverse shear and membrane locking. Thus, transverse shear and membrane locking must be considered simultaneously. Again, for simplicity, we consider a 2D GE element, for which we have three unknowns per node and two constraints per Gauss point. The optimal constraint ratio for the 2D continuous problem is

$$r_{\text{2D}} = \frac{3}{2}. \tag{48}$$

For the discrete problem the discrete constraint ratio reads:

$$r^h_{\text{2D}} = \frac{3p}{2n_g}. \tag{49}$$

Thus, applying URI with $n_g = p$ yields an optimal constraint ratio for the GE elements. Applying URI to the GE elements implies that the rank of the global tangent stiffness is equal to the total number of unknowns, and thus guarantee rank-sufficiency and elements without any zero-energy modes which need to be stabilized.

Even though URI works well independent of the slenderness ratio for elements of polynomial order two and higher, it is well known that the numerical solution gets progressively stiffer for lower order Timoshenko beam (TB) elements compared to the exact one as the

slenderness increases. In order to get an element that is free of locking MacNeal [18, 19] proposed the *residual bending flexibility* (RBF) approach, a device in which the transverse shear stiffness is enhanced by using a substitute reduced shear modulus such that the element reproduces nodally exact solutions independent of the slenderness ratio for a tip loaded straight cantilever beam in the linear regime. In [21], Prathap has shown why the RBF correction yields a correct rate of convergence for linearly interpolated TB elements.

4 NUMERICAL RESULTS

The purpose of the numerical tests is to study the accuracy, performance, robustness and convergence of the GE elements and compare them with 2-noded Euler-Bernoulli (EB) and TB elements based on the CR formulation for the various elements presented in Tab. 1.

All CR elements are based on the formulation proposed by Battini and Pacoste [3, 4]. The EB elements use linear interpolation of the axial displacement and axial rotation about the local beam axis while bending deformations are based on Hermitian cubic shape functions. While the CEBL element is based on classical linear beam theory with only linear terms in the strain expressions, the CEBN element is based on a second order approximation of the Green-Lagrange strains enhanced with a shallow arch definition of the local axial strains to avoid membrane locking. The CEBLS and CEBNS elements are the corresponding EB elements based on the modified Hermitian shape functions accounting for transverse shear deformations. The CR TB elements CTBN and CTBNr are using standard linear interpolation of local displacements and rotations. Except for

Formulation	**Beam theory**	n_n	p	**Strain measure**	**Transverse shear**	**Element name**
Corotational	Euler-Bernoulli	2	1/3	Engineering	No	CEBL
					Yes	CEBLS
				Green-Lagrange	No	CEBN
					Yes	CEBNS
	Timoshenko	2	1	Engineering[1]	Yes	CTBN
						CTBNr[2]
Geometrically exact	Reissner (Timoshenko)	2	1	Biot (Jaumann)	Yes	GEQ1
						GEQ1r[2]
		3	2			GEQ2
		4	3			GEQ3
		5	4			GEQ4
		9	8			GEQ8

Table 1: Various element types compared. [1]Element account for the nonlinear Wagner term in the strain expression. [2]Element has been enhanced with RBF.

the nonlinear Wagner term [31], the strain expression is purely linear for both elements. They utilizes URI to avoid locking and the CTBNr element is further enhanced with RBF to converge to the EB element solution as the slenderness increases.

For each of the various formulations and discretizations considered, the relative error in tip displacement e_u and tip rotation e_θ are chosen as measures of accuracy

$$e_u = \frac{|u^{ref} - u^h|}{|u^{ref}|} \quad \text{and} \quad e_\theta = \frac{|\theta^{ref} - \theta^h|}{|\theta^{ref}|}. \tag{50}$$

The relative error is computed from Eq. (50), where u^{ref} and θ^{ref} are reference solutions obtained with a very fine mesh of eight order GE beam elements.

Since the EB beam elements based on the modified Hermitian shape functions accounting for transverse shear deformations converge to the standard Hermitian interpolated element as the slenderness increases, the comparison between the various TB element formulations are made with the corresponding EB elements accounting for transverse shear deformations. The results obtained for both the linear and the nonlinear EB beam elements accounting for transverse shear almost coincide with those based on the Navier hypothesis for all example problems studied in this paper.

While a few more Newton iterations are needed in the initial than in the final steps for most problems studied, quadratic convergence is obtained in approximately 5 iterations for each step for all discretizations and formulations with a rather tight energy convergence criterion $\varepsilon_E = 10^{-9}$. This also demonstrate that the linearization of the various formulations are consistent. It should also be mentioned that the accuracy and convergence (in the Newton iterations) is independent of the parameterization of the finite rotations.

4.1 Cantilever beam subjected to tip loading

The first example, depicted in Fig. 4, is a straight cantilever beam clamped at one end and subjected to two conservative point loads initially acting in the direction of the local cross-sectional axes at the free end. This example is selected to assess the accuracy and robustness of the various beam formulations under combined bending, shear and torsion when the initial configuration is a straight line. The slenderness ratio for this problem is $\rho_y = L/b = 20$ and $\rho_z = L/h = 40$ for bending in the $xy-$ and $xz-$plane, respectively. The two tip loads are applied over 10 equally sized load increments for all discretizations of the various beam formulations.

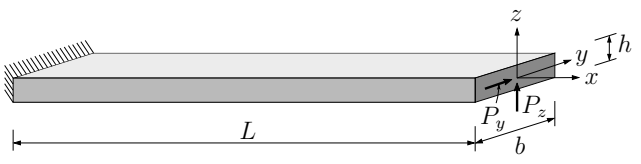

$E = 2.1 \times 10^{11}$
$\nu = 0.3$
$L = 10$
$b = 0.5$
$h = 0.25$
$P_y = 2 \times 10^7$
$P_z = 1 \times 10^7$

Figure 4: Tip loaded cantilever beam: Geometry, loading, boundary conditions and material data.

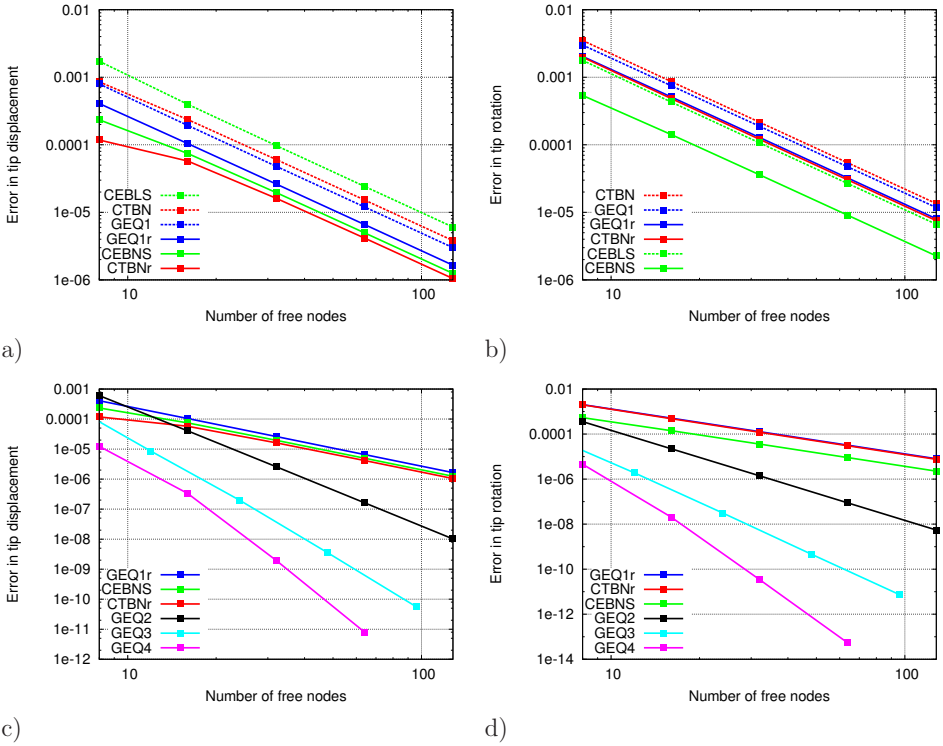

Figure 5: Tip loaded cantilever beam: Relative error in tip displacement and rotation for the various formulations for medium to fine meshes (8–128 free nodes): a) Displacement and b) rotation for all CR- and linear GE-elements, c) displacement and d) rotation for the best CR- and GE-elements of order $p = 1, 2, 3$ and 4.

Fig. 5 shows convergence plots for medium to fine meshes with 8 to 128 free nodes. Firstly, in Figs. 5a and 5b we compare the various EB and linearly interpolated TB elements. It is seen that by adding RBF the error is reduced by a factor of 2 for both the CR and the GE TB elements. We also observe from these figures that for all discretizations with TB elements the accuracy obtained with the CR and the GE formulations are close for the tip displacement and almost coincide for the tip rotation. When comparing the EB and the linearly interpolated TB elements, while the error in tip rotation is almost one order lower for the nonlinear EB element, the accuracy of the tip displacement is of the same order as the linearly interpolated TB elements. We also observe that both the error in tip displacement and rotation is reduced one order when comparing the linear and nonlinear EB elements. Finally, independent of formulation, the convergence order

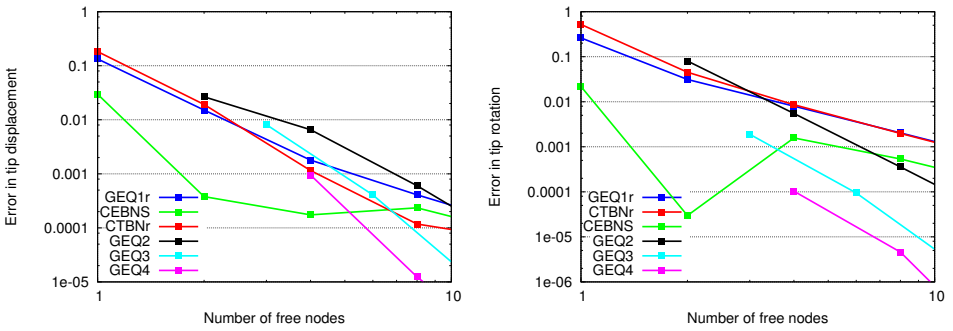

a) b)

Figure 6: Tip loaded cantilever beam: Relative error in tip displacement and rotation for the various formulations for coarse meshes (1–8 free nodes): a) Displacement and b) rotation for the best CR- and GE-elements of order $p = 1, 2, 3$ and 4.

of all 2-noded elements coincide. Next, in Figs. 5c and 5d we compare the best 2-noded elements, i.e. the nonlinear EB and the linearly interpolated TB elements with RBF, with the GE elements of order $p = 2, 3$ and 4. First, we observe as expected that the rate of convergence increases monotonically with polynomial order for both the tip displacement and rotation. We also observe that there is a shift in accuracy of approximately one order when polynomial order is increased.

Fig. 6 shows convergence plots for coarse meshes with 1 to 8 free nodes. We observe that the nonlinear EB element is superior to all other elements for very coarse meshes with 2 to 4 free nodes. However, as the mesh is refined the accuracy of the GE elements of order $p = 2, 3, 4$ is superior to all 2-noded elements.

4.2 Three leg right angle tip loaded space beam

The second example, depicted in Fig. 7, consists of three straight beams, connected at right angles in the reference configuration, such that the beam axis of the three legs are parallel to the $x-$, $y-$ and $z-$axis, respectively. The structure is clamped at one end and subjected to two conservative point loads $P_x = P_z = P$, initially acting in the direction of the negative $x-$ and $z-$axes at the free end. This example was proposed in [25] and has later been revisited in [10], and serves to benchmark nonlinear beam formulations under combined bending, shear and torsion for non-smooth, three-dimensional geometries. The slenderness ratio for this problem is $\rho_y = \rho_z = 10$. The two tip loads are applied over 20 equally sized load increments for all discretizations of the various beam formulations.

In Fig. 8, the displacement and rotation of the tip is plotted versus the load P when each of the three legs are discretized with a uniform mesh of 8 CTBNr and 1024 GEQ8 elements, respectively. We observe that we are not able to distinguish between the results

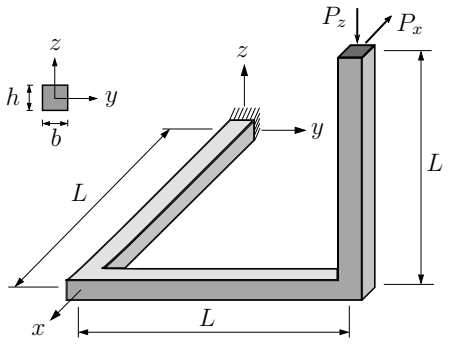

$E = 10^6$
$\nu = 0$
$L = 1$
$b = h = 0.1$
$P_x = P_z = P = 10$

Figure 7: Three leg right angle tip loaded space beam: Geometry, loading, boundary conditions and material data.

obtained with the coarser mesh with 8 CTBNr elements and the reference mesh with 1024 GEQ8 elements.

Analogous to the first example, a convergence plot is given in Fig. 9 to compare the accuracy of the various formulations for meshes with 2 to 32 free nodes per leg. From Figs. 9a and 9b, we observe that the linearly interpolated TB elements enhanced with RBF outperforms the standard formulation. We also observe that the results obtained with the linear EB element CEBLS is indistinguishable from the CR linearly interpolated TB element with added RBF (CTBNr) for all discretizations for both the tip displacement and tip rotation. From the same figures we also observe that independent of formulation

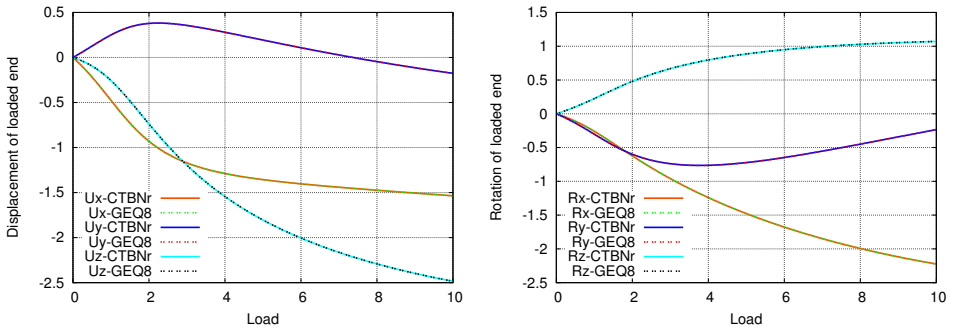

a) b)

Figure 8: Three leg right angle tip loaded space beam: Tip displacement and rotation versus applied load P: a) Displacement and b) rotation for a uniform mesh of 8 CTBNr and 1024 GEQ8 elements per leg, respectively.

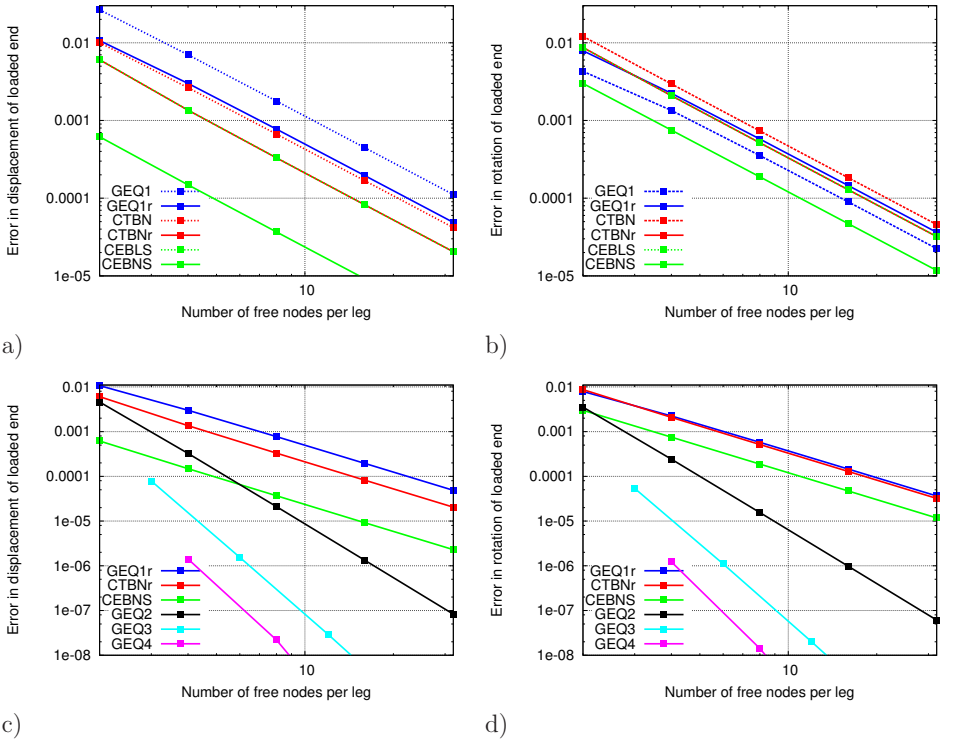

Figure 9: Three leg right angle tip loaded space beam: Relative error in tip displacement and rotation for the various formulations for meshes with 2–32 free nodes per leg: a) Displacement and b) rotation for CR- and linear GE-elements, c) displacement and d) rotation for the best CR- and GE-elements of order $p = 1, 2, 3$ and 4.

the tip displacement for the nonlinear EB element CEBNS is one order more accurate compared with the best linearly interpolated TB elements.

When comparing the best 2-noded elements with GE elements of higher order ($p = 2, 3$ and 4), we observe analogous to the previous example that the rate of convergence for all 2-noded elements coincide while for the higher order GE elements it increases with polynomial order. Also for the GE elements the accuracy is shifted approximately one order as the polynomial order is increased. Again, except for very coarse meshes all higher order GE elements outperform all the 2-noded elements both in terms of accuracy and convergence rate.

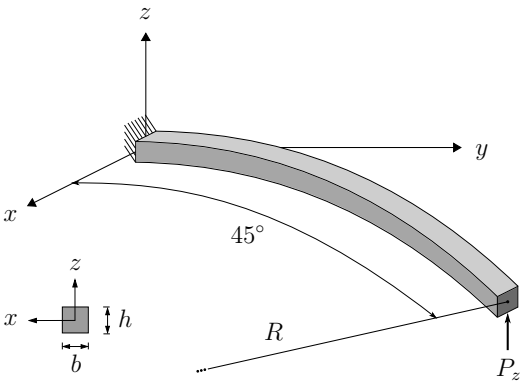

$E = 10^7$
$\nu = 0$
$R = 100$
$b = h = 1$
$P_z = P = 600$

Figure 10: Tip loaded 45° circular cantilever beam: Geometry, loading, boundary conditions and material data.

4.3 Tip loaded 45° circular cantilever beam

In the next example, depicted in Fig. 10, we consider a beam that is curved in its stress-free reference configuration. In particular, 1/8 of a circle with radius R forms the line of centroids that is located in the $xy-$plane in the reference configuration. The curved beam is clamped at one end and subjected to a conservative point load acting in the direction of the $z-$axis in the free end. This problem is a well-established benchmark problem for nonlinear analysis of spatial beams. It was first proposed in [2] and has later been used by a number of authors [5, 6, 7, 9, 10, 15, 25, 28].

Step	Iter	CEBNS	CTBNr	GEQ1r	GEQ2	GEQ3	GEQ4
1	0	4.695×10^{2}	4.695×10^{2}	4.695×10^{2}	4.698×10^{2}	4.698×10^{2}	4.698×10^{2}
	1	8.246×10^{4}	8.239×10^{4}	8.246×10^{4}	8.378×10^{4}	8.379×10^{4}	8.379×10^{4}
	2	1.048×10^{0}	3.918×10^{-1}	2.028×10^{2}	3.188×10^{-1}	3.182×10^{-1}	3.182×10^{-1}
	3	1.131×10^{-3}	9.872×10^{-4}	5.292×10^{-1}	9.649×10^{-4}	9.644×10^{-4}	9.645×10^{-4}
	4	1.441×10^{-8}	1.173×10^{-11}	6.471×10^{-2}	1.646×10^{-7}	1.642×10^{-7}	1.643×10^{-7}
	5	8.382×10^{-17}	3.646×10^{-22}	3.492×10^{-5}	1.192×10^{-14}	1.187×10^{-14}	1.189×10^{-14}
	6			4.949×10^{-10}			
	7			3.572×10^{-21}			
12	0	7.585×10^{1}	7.599×10^{1}	7.597×10^{1}	7.585×10^{1}	7.586×10^{1}	7.586×10^{1}
	1	2.932×10^{2}	2.946×10^{2}	2.946×10^{2}	2.983×10^{2}	2.983×10^{2}	2.983×10^{2}
	2	1.693×10^{-1}	1.695×10^{-1}	1.700×10^{-1}	1.710×10^{-1}	1.710×10^{-1}	1.710×10^{-1}
	3	1.840×10^{-3}	1.847×10^{-3}	1.853×10^{-3}	1.886×10^{-3}	1.886×10^{-3}	1.886×10^{-3}
	4	3.729×10^{-11}	3.343×10^{-11}	2.459×10^{-11}	2.554×10^{-11}	2.554×10^{-11}	2.554×10^{-11}
	5	1.818×10^{-22}	2.053×10^{-22}	5.954×10^{-22}	4.082×10^{-22}	6.091×10^{-22}	8.916×10^{-22}

Table 2: Tip loaded 45° circular cantilever beam: Convergence rates, in the Newton iterations, for the first and final step.

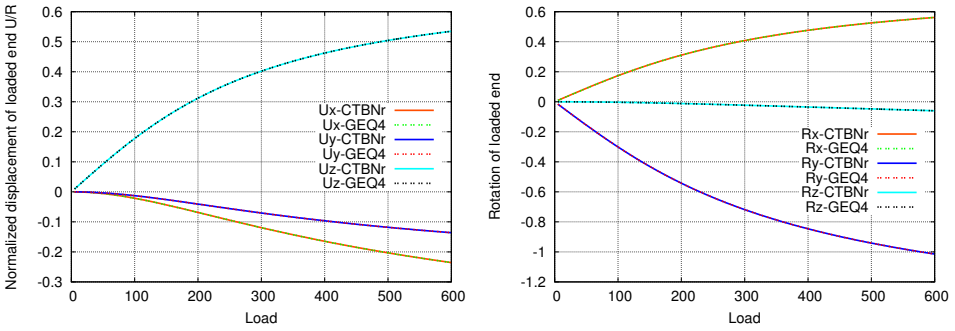

a) b)

Figure 11: Tip loaded 45° circular cantilever beam: Tip displacement and rotation versus applied load P: a) Displacement and b) rotation for a uniform mesh of 8 CTBNr and 1024 GEQ8 elements, respectively.

The tip load is applied over 12 equally sized load increments for all discretizations of the various beam formulations. Tab. 2 shows the convergence rates in terms of energy for the first and last step for the various elements. As shown in Tab. 2, except for the linear interpolated GE element that needs 7 iterations in the initial step, quadratic convergence in the Newton iterations is obtained in 5 iterations for each step for all discretizations and formulations with a rather tight convergence criterion in energy of $\varepsilon_E = 10^{-8}$. All formulations converge to the following displacement and rotation of the loaded end, $u = 59.9984$ and $\theta = 1.16093$. In order to keep the number of unknowns equal for all elements, a uniform mesh of twelve 2-noded elements, six quadratic, four cubic and three quartic elements is used.

In Fig. 11, the normalized displacement and rotation of the tip is plotted versus the load P when the beam is discretized with a uniform mesh of 8 CTBNr and 1024 GEQ4 elements, respectively. As in the previous example, we observe that we are not able to distinguish between the results obtained with the coarser mesh with 8 CTBNr elements and the reference mesh with 1024 GEQ4 elements.

Fig. 12 shows convergence plots for meshes with 2 to 16 free nodes. From Figs. 12b, we observe that independent of formulation the tip rotation for the nonlinear EB element CEBNS is almost one order more accurate compared with the best linearly interpolated TB elements. However, in contrast, from Figs. 12a, we observe that the tip displacement of the CEBNS is less accurate compared with the best linearly interpolated TB elements.

When comparing the best 2-noded elements with GE elements of higher order ($p = 2, 3$ and 4), we observe analogous to the previous example that the rate of convergence for all 2-noded elements coincide while for the higher order GE elements it increases with polynomial order. Also for the GE elements the accuracy is shifted approximately one

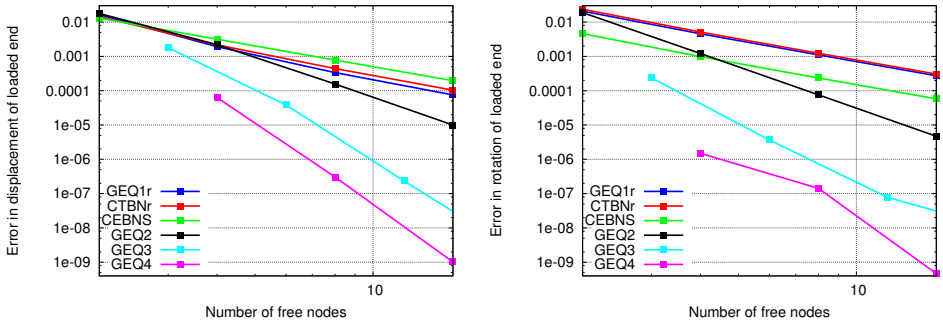

a) b)

Figure 12: Tip loaded 45° circular cantilever beam: Relative error in tip displacement and rotation for the various formulations for meshes with 2–16 free nodes: a) Displacement and b) rotation for the best CR- and GE-elements of order $p = 1, 2, 3$ and 4.

order as the polynomial order is increased. Again, except for the coarsest mesh with 2 free nodes all higher order GE elements outperform all the 2-noded elements both in terms of accuracy and convergence rate. In order to get equal accuracy in tip displacement we need two cubic (36 DOFs), five quadratic (60 DOFS) and 15 linear (90 DOFS) GE elements, 20 TB (120 DOFS) and as much as 30 EB (180 DOFS) CR elements to match the accuracy obtained with one single quartic GE element (24 DOFS). Similarly, as much as three cubic, 11 quadratic, 200 linear GE elements, 200 TB and 100 EB CR elements, is needed to obtain similar accuracy in tip displacement as one quartic GE element. Thus, the accuracy obtained for each DOF invested is much higher for the higher order GE elements compared to all 2-noded elements.

4.4 Tip loaded 90° circular arch

Fig. 13 shows geometry, boundary conditions, loading and material properties for a planar 90° circular arch subjected to a tip shear load P. This problem has also been studied by several other researchers, e.g. Bauer *et al.* [5], however they studied the problem in the linear regime for which there exist a closed form solution, as shown in [5].

Even though the slenderness for this problem, defined as: $R/h = 1000$, is high, the comparison between the various TB element formulations are made with the corresponding EB elements accounting for transverse shear deformations. The tip load is applied over 10 equally sized load increments for all discretizations of the various beam formulations. All formulations converge to the following displacement and rotation of the loaded end, $u = 0.90777806$ and $\theta = 0.99420425$. In Fig. 13, the red curve depicts the final converged configuration.

Fig. 14 shows convergence plots for meshes with 6 to 96 free nodes. When comparing

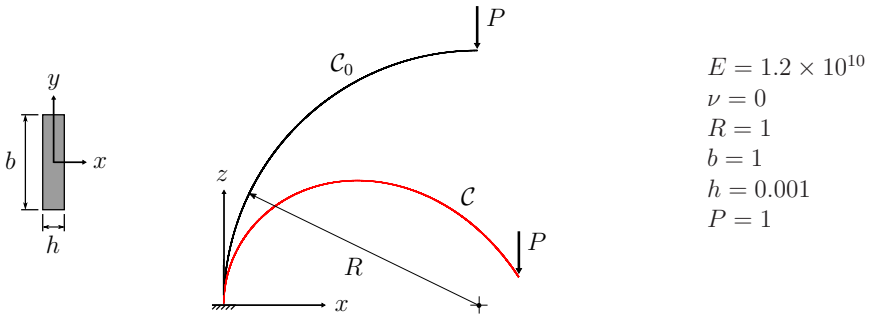

Figure 13: Tip loaded 90° circular cantilever beam: Geometry, loading, boundary conditions and material data.

the best 2-noded elements with GE elements of higher order ($p = 2, 3$ and 4), we observe analogous to the previous example that the rate of convergence for all 2-noded elements coincide while except for the cubic element that exhibit the same convergence as the quadratic element for the higher order GE elements it increases with polynomial order. Furthermore the accuracy is shifted approximately half an order as the number of nodes per element is increased. We also observe that the accuracy and the convergence rate of all discretizations of the CR and the GE 2-noded TB elements, as well as the corotated EB beam with engineering strain are indistinguishable, while the corotated EB beam with Green-Lagrange strain is more accurate both for the tip displacement and the tip rotation. As pointed out in Section 3, both the 2-noded linearly interpolated TB elements based on the GE and the CR formulation denoted GEQ1r and CTBNr have been enhanced with

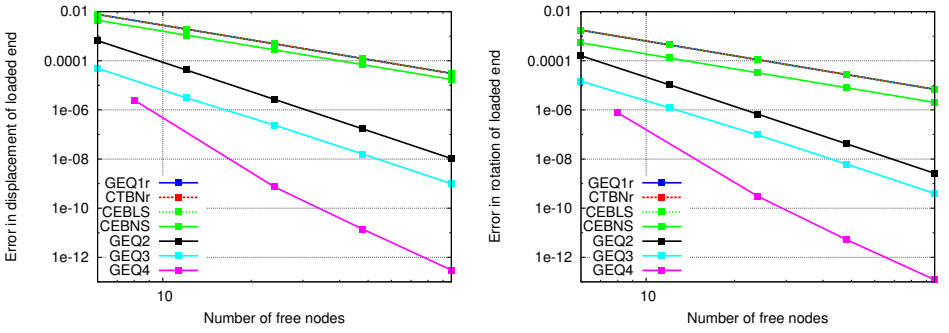

a) b)

Figure 14: Tip loaded 90° circular cantilever beam: Relative error in tip displacement and rotation for the various formulations for meshes with 6–96 free nodes: a) Displacement and b) rotation for the best CR- and GE-elements of order $p = 1, 2, 3$ and 4.

RBF to overcome transverse shear locking as the slenderness increases. The results shown in Fig. 14 demonstrate that the RBF enhancement works very well also in the nonlinear regime for curved geometries in the case of a tip loaded cantilever beam.

5 SUMMARY AND CONCLUDING REMARKS

In this study, we have extended the geometrically exact (GE) beam formulation to an arbitrary order interpolation and compared it with 2-noded Euler-Bernoulli (EB) and Timoshenko beam (TB) elements based on the corotational (CR) formulation, two of the most popular approaches for discretizing nonlinear beams within the context of nonlinear finite element analysis with large displacements and large rotations but small to moderate strains. While these two families of methods have evolved during the last decades and each of them exist with several different enhancements, we have extended the original implementation of the GE formulation as presented in Simo [27] and Simo and Vu-Quoc [28, 29], and the CR formulation proposed by Battini and Pacoste [3, 4]. Both formulations may be extended to non-linear material models (inelastic or plastic), interfacing with other types of structural elements and extended to nonlinear dynamic analysis.

The higher order GE beam elements are the formulation of choice when performance and accuracy are crucial. Despite their complexity, both theoretical and numerical, our study reveals that for the same CPU cost, the elements provide significantly more accurate results than any of the 2-noded CR elements. It turns out that the CPU cost involved in the computation of the higher order GE elements is not significantly higher due to increased number of integration points and DOFS per element. As shown in Helgedagsrud *et al.* [12], the per-degree-of-freedom accuracy of GE beam elements may be even further improved by replacing the Lagrangian FE functions with isogeometric analysis (IGA) based on non-uniform rational B-splines (NURBS) [8, 14, 22].

In spite that we have used a symmetrized tangent stiffness for all GE elements and nonsymmetric tangent stiffness for all CR elements, they all exhibit a quadratic rate of convergence in the Newton iterations. Our numerical study also demonstrates that the accuracy, the number of Newton iterations, and the computational cost is independent of the parameterization of the finite rotations for both formulations.

Another observation is that it is highly recommended to enhance the linearly interpolated 2-noded TB elements with residual bending flexibility whether it is based on the GE or the CR formulation. Furthermore, we cannot claim the superiority of one approach over the other when we restrict our study to 2-noded TB elements. However, among the 2-noded elements, the nonlinear 2-noded cubic interpolated EB element based on the CR approach enhanced with the shallow arch terms exhibit superior accuracy. Modifying the Hermitian shape functions to account for transverse shear deformations, this element allows for a significant reduction of elements used to discretize the structure compared to all other 2-noded elements studied.

6 ACKNOWLEDGEMENT

The first author would like to also acknowledge the support and helpful comments from Professor in Structural Mechanics Jean-Marc Battini at Department of Civil and Architectural Engineering at the Royal Institute of Technology (KTH) in Stockholm, Sweden.

REFERENCES

[1] Auricchio, F., Carotenuto, P. and Reali, A. On the geometrically exact beam model: A consistent, effective and simple derivation from three-dimensional finite-elasticity. *Int. J. Solids. Struct.* (2008) **45**:4766–4781.

[2] Bathe, K.J. and Belourchi, S. Large displacement analysis of three-dimensional beam structures. *Int. J. Numer. Meth. Engrg.* (1979) **14**:961–986.

[3] Battini, J.-M. and Pacoste, C. Co-rotational beam elements with warping effects in instability problems. *Comput. Meth. Appl. Mech. Engrg.* (2002) **191**:1755–1789.

[4] Battini, J.-M. and Pacoste, C. Plastic instability of beam structures using co-rotational elements. *Comput. Meth. Appl. Mech. Engrg.* (2002) **191**:5811–5831.

[5] Bauer, A.M., Breitenberger, M., Philipp, B., Wüchner, R. and Bletzinger, K.-U. Nonlinear isogeometric spatial Bernoulli beam. *Comput. Meth. Appl. Mech. Engrg.* (2016) **303**:101–127.

[6] Betsch, P. and Steinmann, P. Frame-indifferent beam finite elements based upon the geometrically exact beam theory. *Comput. Meth. Appl. Mech. Engrg.* (2002) **54**:1775–1788.

[7] Cardona, A. and Géradin, M. A beam finite element non-linear theory with finite rotations. *Int. J. Numer. Meth. Engrg.* (1988) **26**:2403–2438.

[8] Cottrell, J.A., Hughes, T.J..R. and Bazilevs Y. *Isogeometric Analysis: Toward Integration of CAD and FEA*. John Wiley & Sons, Chichester, England, (2009).

[9] Crisfield, M. A consistent corotational formulation for non-linear, three-dimensional beam elements. *Comput. Meth. Appl. Mech. Engrg.* (1990) **81**:131–150.

[10] Eugster, S.R., Hesch, C., Betsch, P. and Glocker, Ch. Director-based beam finite elements relying on the geometrically exact beam theory formulated in skew coordinates. *Int. J. Numer. Meth. Engrg.* (2014) **97**:111–129.

[11] Felippa, C.A. and Haugen, B. A unified formulation of small-strain corotational finite elements: I. Theory *Comput. Meth. Appl. Mech. Engrg.* (2005) **194**:2285–2335.

[12] Helgedagsrud, T.A., Raknes, S.B. and Mathisen, K.M. On locking-free methods for isogeometric large deformation analysis of geometrically exact three-dimensional beams. *Proc. 8. Nat. Conf. Comput. Mech. (MekIT'15)*, Skallerud, B., and Andersson, H.I. (Eds.), CIMNE, Barcelona, Spain (2015) pp. 167–201.

[13] Hughes, T.J.R. *The Finite Element Method*. Prentice–Hall, Englewood Cliffs, NJ, USA, (1987).

[14] Hughes, T.J.R., Cottrell, J.A. and Bazilevs, Y. Isogeometric Analysis: CAD, Finite Elements, NURBS, Exact Geometry and Mesh Refinement. *Comput. Meth. Appl. Mech. Engrg.* (2005) **194**:4135–4195.

[15] Ibrahimbegović, A. and Frey, F. Finite element analysis of linear and nonlinear planar deformations of elastic initially curved elements. *Int. J. Numer. Meth. Engrg.* (1992) **36**:3239–3258.

[16] Ibrahimbegović, A. On finite element implementation of geometrically nonlinear Reissner's beam theory: Three-dimensional curved beam elements. *Comput. Meth. Appl. Mech. Engrg.* (1995) **122**:11–26.

[17] Ibrahimbegović, A., Frey, F. and Kožar, I. Computational aspects of vector-like parameterization of three-dimensional finite rotations. *Int. J. Numer. Meth. Engrg.* (1995) **38**:3653–3673.

[18] MacNeal, R.H. A simple quadrilateral plate element. *Comput. Struct.* (1978) **8**:175–183.

[19] MacNeal, R.H. *Finite Elements: Their Design and Performance*. Marcel Dekker, New York, USA, (1994).

[20] Mathisen, K.M. and Bergan, P.G. Large displacement analysis of submerged multibody systems. *Engrg. Comput.* (1992) **9**:609–634.

[21] Prathap, G. The variationally correct rate of convergence for a two-noded beam element, or why residual bending flexibility corrections is an extravariational trick. *Commun. Numer. Meth. Engrg.* (1995) **11**:403–407.

[22] Raknes, S.B., Deng, X., Bazilevs, Y., Benson, D.J., Mathisen, K.M. and Kvamsdal, T. Isogeometric rotation-free bending-stabilized cables: Statics, dynamics, bending strips and coupling with shells. *Comput. Meth. Appl. Mech. Engrg.* (2013) **263**:127–143.

[23] Reissner, E. On one-dimensional finite-strain beam theory: The plane problem. *J. Appl. Math. Phys.* (1972) **32**:795–804.

[24] Reissner, E. On finite deformations of space curved beams. *J. Appl. Math. Phys.* (1981) **32**:734–744.

[25] Romero, I. A comparison of finite elements for nonlinear beams: The absolute nodal coordinate and geometrically exact formulations. *Multibody System Dynamics* (2008) **20**:51–68.

[26] Saje, M. Finite element formulation of finite planar deformation of curved elastic beams. *Comput. Struct.* (1991) **39**:327–337.

[27] Simo, J.C. A finite strain beam formulation. The three-dimensional dynamic problem. Part I. *Comput. Meth. Appl. Mech. Engrg.* (1985) **49**:55–70.

[28] Simo, J.C. and Vu-Quoc, L. A three-dimensional finite strain rod model. Part II: Computational aspects. *Comput. Meth. Appl. Mech. Engrg.* (1986) **58**:79–116.

[29] Simo, J.C. Vu-Quoc, L. A geometrically-exact rod model incorporating shear and torsion-warping deformation. *Int. J. Solids. Struct.* (1991) **27**:371–393.

[30] Stolarski, H. and Belytschko, T. Shear and membrane locking in curved C^0 elements. *Comput. Meth. Appl. Mech. Engrg.* (1983) **41**:279–296.

[31] Wagner, H. *Verdrehung und Knickung von offenen Profilen (Torsion and buckling of open sections)*. 25th Anniversary Publication, Technische Hochschule, Danzig (2nd ed.), NACA translation, Technical memo No. 807, Washington DC, USA, (1936).